International Journal of Heat and Mass Transfer 201 (2023) 123624

Contents lists available at ScienceDirect

International Journal of Heat and Mass Transfer

journal homepage: www.elsevier.com/locate/hmt

# A hybrid Monte Carlo-discrete ordinates method for phonon transport in micro/nanosystems with rough interfaces

Xin Ran[1], Yunfan Huang[1], Moran Wang*

*Key Laboratory for Thermal Science and Power Engineering of Ministry of Education, Department of Engineering Mechanics, Tsinghua University, Beijing 100084, China*

ARTICLE INFO

*Article history:*
Received 28 July 2022
Revised 19 October 2022
Accepted 31 October 2022
Available online 11 November 2022

*Keywords:*
Hybrid method
Monte Carlo method
Discrete ordinates method
Micro/nano-scale heat transport
Phonon transport

ABSTRACT

In recent years, the rapid development of micro/nanosystems raises the demand of thermal optimization of the new designs, and thus the accurate and efficient prediction of phonon transport in mesoscopic systems with complex interfaces is required. This work proposes a hybrid Monte Carlo-discrete ordinates method (MC-DOM) for steady-state phonon transport in such systems by developing an algorithm to exchange information between MC and DOM subdomains. Based on the phonon Boltzmann transport equation which is physically compatible with the system scale, our formulation exploits the computational efficiency of DOM in the bulk region with flexibility of MC near complex interfaces. The cross-plane phonon transport through the thin films is considered first as the benchmark for method verification, whose results agree well with those calculated by numerical and analytical solutions. It is noteworthy that compared to MC as a pure particle method, the hybrid method runs faster over a hundred of times for the temperature calculation when high-precision results are needed. The hybrid method is then applied to simulate the in-plane phonon transport through the double-layer thin films with rough interfaces. It is found that for rectangular interfaces with different roughness, the interfaces perpendicular to the heat flux will cause a larger thermal resistance than the parallel ones. Our hybrid method enriches numerical tools for mesoscopic phonon transport simulation, and is helpful to reveal the mechanisms behind and optimize the heat transport in micro/nanosystems with complex geometries.



## 1. Introduction

The mechanism of heat transport at micro/nanoscale becomes more and more important for optimized thermal designs of micro/nano devices, such as electronics and thermoelectrics [1,2]. At a small scale, the contribution from interfaces is non-negligible and the classical law of heat conduction may fail [3–6], which makes it essential to study the interfacial heat transport at micro/nanoscale beyond Fourier's law. In this work, we focus on the steady-state phonon transport in mesoscopic systems with a geometrically bulk region and complex interfaces (such as dislocation, roughness and grain boundary), considering that such systems are often encountered in engineering applications and the phonon acts as the major heat carrier in the traditional semiconductor devices.

The main challenge of simulating such systems originates from the coupling complexity of mesoscopic physics modeling and complex interface treatment. Physically, the phonon transport in the whole mesoscopic system is dramatically impacted by the system boundary/interface and shows a ballistic(-diffusive) behavior, which means the region where kinetic effects are important is no longer sufficiently localized and small, making the diffusion formulation no longer valid even in the geometrically bulk region [7]. Thus, those hybrid methods based on domain decomposition and utilizing the deterministic macroscopic equations in the bulk region, such as the diffusion equation solver for bulk heat transfer coupled with special interfacial solver (as the counterpart of those for fluid flow [8–10]), will not be applicable for such systems [11–14], while other efforts incorporating thermal fluctuations into macroscopic hydrodynamic formulation provides a useful approximation rather than the actual variance of the heat flux which cannot be utilized to capture the details of phonon transport, such as fluctuating hydrodynamics and dissipative particle dynamics [15–17]. Besides, first principles calculations such as molecular dynamics simulations are too expensive for treating phonon transport at the mesoscopic scales [18–21]. Thus, a kinetic description based on the phonon Boltzmann transport equation (BTE) offers a reasonable balance between physical fidelity and modeling complexity and is able to accurately describe the phonon transport behavior as the characteristic length scales of the system approach the

* Corresponding author
*E-mail address:* mrwang@tsinghua.edu.cn (M. Wang).
[1] The first two authors contribute equally to the work.

https://doi.org/10.1016/j.ijheatmasstransfer.2022.123624
0017-9310/

phonon mean free path. However, it is not an easy task to obtain the solution of BTE, especially when it comes to the system with a complex geometry. This leads to the second issue, i.e., the numerical treatment of rough interfaces.

Two branches of BTE solvers have been developed, i.e., discretization-based deterministic ones and particle-based stochastic ones [22,23]. The former ones may include lattice Boltzmann method (LBM) [24–26], discrete kinetic scheme (DUGKS) [27–29], discrete ordinates method (DOM) [30–33] and others [34], while the latter ones mainly refer to the Monte Carlo methods (MC), covering from the gas, phonon, and photon transport [35–42] to the hybrid simulation of electron-phonon coupled transport [43–46]. Though the high dimensionality of the distribution function adds the computational costs for discretization, the deterministic characteristics enable those methods to simulate phonon transport with a high precision within the bulk regions, but usually shows a poor performance near the complex interfaces due to the required additional special treatment such as boundary mesh refinement, which is often the case for DOM and DUGKS with relatively dense discrete points in angular discretization, while LBM has a rather simple boundary treatment formulation but compromises with less accuracy. On the other hand, particle-based methods could naturally simulate advection processes without stability issues, which makes them particularly appealing to capture the interfacial behavior of incoherent phonons. However, MC methods suffer from enormous computational costs from the large number of required computational particles to suppress the statistical fluctuations emerging from the relatively large bulk parts of the system [23].

This work proposes a hybrid method coupling MC and DOM in a manner of domain decomposition to simulate the phonon transport in mesoscopic systems with complex interfaces, which embeds the deviational MC method within a BTE-based continuum grid by considering the detailed energy conservation in each phase element. It enables particle-based treatments to capture the phonon behaviors near the small region of complex interfaces, while simulating the phonon transport in the large bulk region in a deterministic way which leads to a better balance of accuracy and efficiency. A novel algorithm for the information exchange at the interface between the MC and DOM subdomains is proposed based on the formulation of cumulative distributions, and the individual methods inside the MC and DOM subdomain in the present study follow the author's previous works [47–49]. Specifically, the energy-based deviational formulations of MC method based on the linearized phonon BTE is used to reduce the statistical variation, ensure the exact energy conservation and acquire additional computational benefits [50,51], and the steady-state scheme under the small temperature difference (so called the "kinetic-type" MC) is adopted in developing the present hybrid method to avoid extra simulation for the transient evolution [52,53]. To match the deviational MC formulation, an intensity-based deviational steady-state equation of phonon radiative transfer in the geometrically bulk region is solved by phonon DOM, with the Gauss-Legendre quadrature used in frequency domain to improve the algorithm efficiency compared to the uniform discretization [7,33,48]. Though the hybrid MC-DOM algorithm has been developed for neutron and photon transport and applied to the radiation shielding problems [54–56], the formulation for phonon transport has rarely been reported yet. Our hybrid scheme provides an accurate and efficient way to deal with the ballistic-diffusive phonon transport inside the complex geometries.

In this work, we will mainly focus on the coupling model development and method verification, and preliminarily showcase our performance advantage and wide applicability. The remaining part of this article is organized as follows. Section 2 gives the formulation of hybrid MC-DOM modeling, containing the phonon BTE-based formulations of the elementary intensity-based DOM and energy-based MC methods and information exchanging algorithm at the interface between the DOM and MC subdomains. The verifications of the new hybrid method are given in Section 3, in which we consider the one-dimensional (1D) cross-plane phonon transport through the single/double-layer thin films, and the algorithm efficiency is compared with a pure Monte Carlo method and discussed regarding the former case. The hybrid method is finally applied to the two-dimensional (2D) in-plane phonon transport through a single-layer thin film and the double-layer thin film with rough interface in between in Section 4. Conclusions of this work is presented in Section 5. The numerical details of deviational DOM algorithm in low-dimensional systems are listed in Appendix A.

## 2. Formulation of Hybrid MC-DOM Modeling

In this section, the mathematical formulation of proposed hybrid MC-DOM modeling is introduced. Since our whole method stands on the basis of phonon BTE with singe-relaxation-time (SRT) approximation, the phonon BTE-based formulation as well as its deviational intensity-based and energy-based equivalent forms is presented first. Then comes the coupling scheme of our hybrid model, with the special attention on the information exchanging algorithm at the interface between DOM and MC domains (referred as the "contact interface" in this article).

### 2.1. Phonon BTE-based formulation

#### 2.1.1. Phonon BTE with SRT approximation

The phonon BTE with SRT approximation reads [57]

$$\frac{\partial f}{\partial t}+\mathbf{v}_{\mathrm{g}}(\omega,\mathrm{p})\cdot\nabla f=-\frac{f-f_{\mathrm{pse}}^{\mathrm{eq}}\left(T_{\mathrm{pse}}^{\mathrm{eq}}\right)}{\tau(\omega,\mathrm{p},T)}, \tag{1}$$

where $f=f(\mathbf{x},t,\mathbf{k},\mathrm{p})$ is the phonon number density distribution, with $\mathbf{x}$ representing the position vector, $t$ the time, $\omega$ the angular frequency, $\mathbf{k}$ the phonon wave vector and p the polarization; $\mathbf{v}_{\mathrm{g}}(\omega,\mathrm{p})=\nabla_{\mathbf{k}}\omega(\mathbf{k},\mathrm{p})$ and $\tau(\omega,\mathrm{p},T)$ are the frequency-dependent group velocity and relaxation time of phonons; $f_{\mathrm{pse}}^{\mathrm{eq}}\equiv f^{\mathrm{eq}}(\omega,T_{\mathrm{pse}}^{\mathrm{eq}})=1/[\exp(\hbar\omega/k_{\mathrm{B}}T_{\mathrm{pse}}^{\mathrm{eq}})-1]$ denotes the pseudo-equilibrium phonon distribution at the pseudo-equilibrium temperature $T_{\mathrm{pse}}^{\mathrm{eq}}$. The equilibrium temperature $T$ and pseudo-equilibrium temperature are defined at each time and position by the local energy and pseudo-energy conservation

$$\sum_{\mathrm{p}}\int\hbar\omega(f(\omega,\mathrm{p})-f^{\mathrm{eq}}(\omega,T))D(\omega,\mathrm{p})d^3\boldsymbol{\omega}=0 \tag{2}$$

$$\sum_{\mathrm{p}}\int\frac{\hbar\omega}{\tau(\omega,\mathrm{p},T)}\left(f(\omega,\mathrm{p})-f^{\mathrm{eq}}\left(\omega,T_{\mathrm{pse}}^{\mathrm{eq}}\right)\right)D(\omega,\mathrm{p})d^3\boldsymbol{\omega}=0 \tag{3}$$

where $D(\omega,\mathrm{p})=k^2/(2\pi^2v_{\mathrm{g}})$ denotes the density of states for three-dimensional materials and $v_{\mathrm{g}}$ the magnitude of the phonon group velocity.

Three materials are treated in the present work, including Si, Al, and Ge, with the dispersion properties referred to Refs. [58,59], and [60] respectively. The acoustic and optical modes are considered for both Si and Ge, while Al has the acoustic modes only. The expressions of relaxation times of Si and Ge are both referred to Ref. [61]. Specifically, the impurity and Umklapp relaxation times are given by $\tau_{\mathrm{I}}^{-1}=A_{\mathrm{I}}\omega^4$ and $\tau_{\mathrm{U}}^{-1}=B_{\mathrm{U}}T\omega^2\exp(-C_{\mathrm{U}}/T)$, and the normal relaxation times for transverse and longitudinal modes are given by $\tau_{\mathrm{TN}}^{-1}=B_{\mathrm{TN}}\omega T^4$ and $\tau_{\mathrm{LN}}^{-1}=B_{\mathrm{LN}}\omega^2T^3$, respectively. The parameter for impurity relaxation time is derived analytically [62,63], while the others including the boundary relaxation time $\tau_{\mathrm{B}}$ are obtained by fitting the bulk thermal conductivities throughout 0-300 K, as listed in Table 1. The relaxation time for Al is set to $8.95\times10^{-12}$ s to fit the lattice thermal conductivity in Ref. [64].

**Table 1**
Fitting parameters for various relaxation times of Si and Ge.

| Material | $A_{\mathrm{I}}$ | $B_{\mathrm{U}}$ | $C_{\mathrm{U}}$ | $B_{\mathrm{TN}}$ | $B_{\mathrm{LN}}$ | $\tau_{\mathrm{B}}^{-1}$ |
|---|---|---|---|---|---|---|
| Si | $1.32 \times 10^{-45}$ s$^3$ | $1.00 \times 10^{-19}$ s/K$^3$ | 120 K | $1.00 \times 10^{-16}$ K$^{-4}$ | $5.00 \times 10^{-25}$ s/K | $1.16 \times 10^{6}$ s$^{-1}$ |
| Ge | $2.40 \times 10^{-44}$ s$^3$ | $8.50 \times 10^{-20}$ s/K$^3$ | 32 K | $6.80 \times 10^{-14}$ K$^{-4}$ | $2.50 \times 10^{-25}$ s/K | $0.27 \times 10^{6}$ s$^{-1}$ |

In this work, the equivalent deviational forms of the steady-state phonon BTE Eq. (1) are solved by DOM and MC in different subdomains, which will be introduced in the following parts.

### 2.1.2. Intensity-based deviational DOM

The equation of phonon radiative transfer to be solved by DOM reads [65]

$$\frac{\partial I}{\partial t} + \mathbf{v}_{\mathrm{g}}(\omega, \mathrm{p}) \cdot \nabla I = -\frac{I - I_{\mathrm{pse}}^{\mathrm{eq}}\left(T_{\mathrm{pse}}^{\mathrm{eq}}\right)}{\tau(\omega, \mathrm{p}, T)}, \tag{4}$$

with the phonon intensity $I = \hbar\omega f D(\omega, \mathrm{p}) v_{\mathrm{g}}(\omega, \mathrm{p})/4\pi$ and the pseudo-equilibrium phonon intensity $I_{\mathrm{pse}}^{\mathrm{eq}} = \hbar\omega f_{\mathrm{pse}}^{\mathrm{eq}} D(\omega, \mathrm{p}) v_{\mathrm{g}}(\omega, \mathrm{p})/4\pi$. To match the phonon transport problem that we are concerned about and the deviational MC method presented in the next part, the steady-state deviational version of Eq. (4) is introduced

$$\mathbf{v}_{\mathrm{g}}(\omega, \mathrm{p}) \cdot \nabla I^{\mathrm{d}} = -\frac{I^{\mathrm{d}} - \left(I_{\mathrm{pse}}^{\mathrm{eq}}\left(T_{\mathrm{pse}}^{\mathrm{eq}}\right) - I_{\mathrm{ref}}^{\mathrm{eq}}\left(T_{\mathrm{ref}}^{\mathrm{eq}}\right)\right)}{\tau(\omega, \mathrm{p}, T)}, \tag{5}$$

where $I^{\mathrm{d}} = \hbar\omega(f - f_{\mathrm{ref}}^{\mathrm{eq}}) D(\omega, \mathrm{p}) v_{\mathrm{g}}(\omega, \mathrm{p})/4\pi$ is the phonon deviational intensity, and $I_{\mathrm{ref}}^{\mathrm{eq}} = \hbar\omega f_{\mathrm{ref}}^{\mathrm{eq}} D(\omega, \mathrm{p}) v_{\mathrm{g}}(\omega, \mathrm{p})/4\pi$ the reference equilibrium phonon intensity, with the reference equilibrium phonon distribution $f_{\mathrm{ref}}^{\mathrm{eq}}$ at the reference equilibrium temperature $T_{\mathrm{ref}}^{\mathrm{eq}}$ prescribed before each simulation.

In the DOM algorithm, the spatial, angular, and frequency domains are first discretized into $I_{i,u,j,l,m,\mathrm{p}}^{\mathrm{d}} \equiv I^{\mathrm{d}}(x_i, y_u, \theta_j, \varphi_l, \omega_m, \mathrm{p})$, where $(x_i, y_u)$ denotes the spatial grid point, $\theta_j$ the polar angle, $\varphi_l$ the azimuth angle, $\omega_m$ the frequency, and p the polarization. Then, Eq. (5) is solved by the finite difference method on the grid points which is quite similar to the numerical techniques used in computational fluid dynamics, and the semi-implicit upwind scheme for a stable iteration of spatial derivative terms is adopted in the present study [33]. Once the phonon intensities at discretized points obtained, the macroscopic variables can be calculated by summing these intensities with certain weights. For 1D cases, the statistical formulation reads

$$T = \frac{2\pi}{C_V} \sum_{j,m,\mathrm{p}} \frac{I^{\mathrm{d}}\left(\mathrm{p}, \omega_m, \mu_j\right)}{v_{\mathrm{g}}(\mathrm{p}, \omega_m)} \varpi_m w_j + T_{\mathrm{ref}}^{\mathrm{eq}}, \tag{6}$$

$$q = 2\pi \sum_{j,m,\mathrm{p}} I^{\mathrm{d}}\left(\mathrm{p}, \omega_m, \mu_j\right) \mu_j \varpi_m w_j, \tag{7}$$

where $C_V$ is the volume heat capacity, and $\mu_j = \cos\theta_j$. The Gauss-Legendre discretization for a fast and accurate integration is adopted in the present study [47]. The variation of the macroscopic variables between the contiguous iterations are also used as the criteria of convergence in the simulation. For the detailed iteration schemes of 1D and 2D cases utilized in the next sections, see the Appendix A.

Three types of boundary conditions should be addressed here. For the constant temperature boundary, considering a 1D problem with the node 1 located at the left boundary (L) with constant temperature $T_{\mathrm{L}}$, the boundary condition reads

$$\left(I_{1,j,m,\mathrm{p}}^{\mathrm{d}}\right)_{\mathrm{L}} = \frac{v_{\mathrm{g}}(\omega_m, \mathrm{p}) C_{\omega_m}\left(T_{\mathrm{L}} - T_{\mathrm{ref}}^{\mathrm{eq}}\right)}{4\pi}, \tag{8}$$

where $C_\omega = \hbar\omega D(\omega, \mathrm{p}) \frac{\partial f}{\partial T}|_{T^0}$ is the volume heat capacity per unit frequency at equilibrium temperature $T^0$, which is equal to the reference equilibrium temperature here. The assumption of the small temperature difference has been used in deriving Eq. (8). For the adiabatic diffuse boundary at the upper boundary (U) in a 2D problem, the boundary condition is written as

$$\int_{\mathbf{m}\cdot\mathbf{n}_y<0} I^{\mathrm{d}}\mathbf{m} \cdot \mathbf{n}_y \mathrm{d}\Omega = -\int_{\mathbf{m}\cdot\mathbf{n}_y>0} I^{\mathrm{d}}\mathbf{m} \cdot \mathbf{n}_y \mathrm{d}\Omega, \tag{9}$$

where $\mathbf{m}=\mathbf{v}_{\mathrm{g}}/v_{\mathrm{g}}$ represents the unit vector at the direction of group velocity, $\mathbf{n}_y$ the unit vector along the $y$ direction, and $\Omega$ the solid angle. The phonon deviational intensities are distributed uniformly in all directions for $\mathbf{m} \cdot \mathbf{n}_y < 0$ based on the assumption of complete diffuse scattering, which leads to the discretized form of Eq. (9)

$$\left(I_{i,M,j,l,m,\mathrm{p}}^{\mathrm{d}}\right)_{\mathrm{U}} = -\frac{\sum_l \sum_j \left(I_{i,M,j,l,m,\mathrm{p}}^{\mathrm{d}}\right)_{\mathrm{U}} \sin\varphi_l \sqrt{1-\mu_j^2} w_j \xi_l}{\pi}, \tag{10}$$

where the summations over $j$ and $l$ at the right side of the equation correspond to the discrete points satisfying $\mathbf{m} \cdot \mathbf{n}_y > 0$, and $w_i\sqrt{1-\mu_i^2}$ ($\zeta_l \sin\varphi_l$) the weights of $\theta_j$ ($\varphi_l$). For the periodic heat flux boundaries between the left (L) and right (R) boundaries, the distribution deviations from the local equilibrium distributions are required to be periodic. Since the external temperature gradient has been considered in the prescribed reference equilibrium temperature, the periodic heat flux boundary condition can be realized by specifying the phonon deviational intensities to be equal to each other at each polarization, frequency, and direction, i.e., $\left(I_{1,u,j,l,m,\mathrm{p}}^{\mathrm{d}}\right)_{\mathrm{L}} = \left(I_{N,u,j,l,m,\mathrm{p}}^{\mathrm{d}}\right)_{\mathrm{R}}$.

### 2.1.3. Energy-based deviational MC

The steady-state energy-based deviational phonon BTE to be solved by MC has been developed recently [50,51,66]

$$\mathbf{v}_{\mathrm{g}}(\omega, \mathrm{p}) \cdot \nabla e^{\mathrm{d}} = -\frac{e^{\mathrm{d}} - \left(e_{\mathrm{pse}}^{\mathrm{eq}}\left(T_{\mathrm{pse}}^{\mathrm{eq}}\right) - e_{\mathrm{ref}}^{\mathrm{eq}}\left(T_{\mathrm{ref}}^{\mathrm{eq}}\right)\right)}{\tau(\omega, \mathrm{p}, T)} \tag{11}$$

where $e^{\mathrm{d}} = \hbar\omega(f - f_{\mathrm{ref}}^{\mathrm{eq}})$ represents the phonon deviational energy, $e_{\mathrm{pse}}^{\mathrm{eq}} = \hbar\omega f_{\mathrm{pse}}^{\mathrm{eq}}$ the pseudo-equilibrium phonon energy, and $e_{\mathrm{ref}}^{\mathrm{eq}} = \hbar\omega f_{\mathrm{ref}}^{\mathrm{eq}}$ the reference equilibrium phonon energy. As stated in the introduction part, quite a few computational benefits are gained from the above formulation, such as variance reduction, exact energy conservation, and additional efficiency enhancement.

The linearized version of Eq. (11) is actually solved under tiny temperature difference assumption in the kinetic MC scheme, in which the energy packets with an effective deviational energy $\varepsilon_{\mathrm{eff}}^{\mathrm{d}}$ are treated independently along their trajectories accumulated by linear segments separated by several types of scatterings. Specifically, the computational particle, each representing an energy packet, is emitted from the heat source one by one and tracked until the particle exits the isothermal boundary or the simulation time domain. During the tracking, the computational particle may encounter boundary, interface, and intrinsic scatterings and its contributions on macroscopic information is recorded. After all the computational particles tracked, the macroscopic information can be obtained statistically based on those contributions. For the steady-state scheme of kinetic-type MC method considered in the

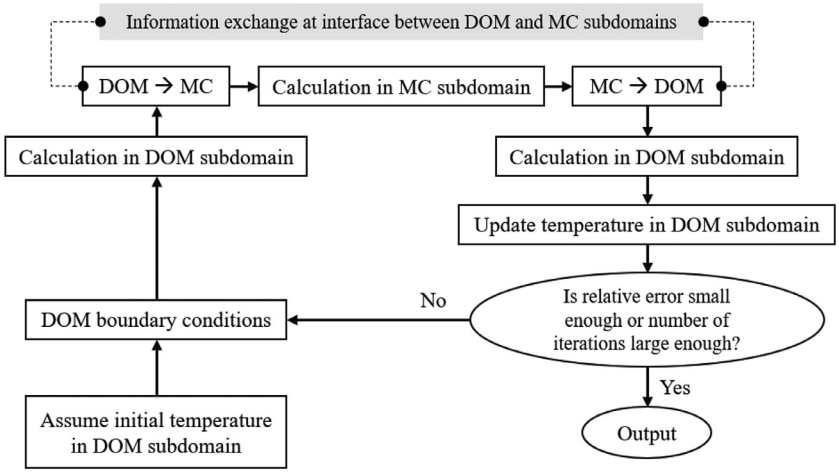


**Fig. 1.** Flow chart of the hybrid MC-DOM for phonon transport.

present work, the temperature and the heat flux can be obtained as follows [51,52,66]

$$T=\frac{1}{C_V}\sum_{i_0=1}^{N}\sigma_{i_0}\varepsilon_{\text{eff}}\tau+T_{\text{ref}}^{\text{eq}}, \tag{12}$$

$$q=\sum_{i_0=1}^{N}\eta_{\mu}\sigma_{i_0}\varepsilon_{\text{eff}}, \tag{13}$$

where $\sigma_{i_0}$ is the sign of the $i_0$-th energy packet in MC method, $\varepsilon_{\text{eff}}$ the effective energy rate of one energy packet [66], $\eta_{\mu}$ the sign of the velocity vector projection in the positive direction of the heat flux, and $N$ the total number of all energy packets colliding with the interface normal to the heat flux direction. See Refs. [47,48,67] for more detailed introductions.

### 2.2. MC-DOM coupling scheme

As a hybrid atomistic-continuum method based on domain decomposition, the key point to the MC-DOM coupling scheme is to develop a numerical algorithm to exchange information between DOM and MC subdomains. The main idea of our treatment is as follows. Since the phonon intensity calculated in the DOM subdomains and the properties of computational particle (energy packet) calculated in the MC subdomains should obey the "detailed energy conservation" within each phase element at the contact interface in between, i.e., the both sides share the same distribution of phonon properties, an algorithm for information exchange is proposed on the basis of the multidimensional cumulative distributions at the contact interface. In this subsection, the coupling framework of hybrid MC-DOM method is introduced first, and then the detailed information exchanging algorithm.

#### 2.2.1. Coupling framework of hybrid MC-DOM method

The coupling framework of our hybrid method is presented in Fig. 1. First, initialize the pseudo-equilibrium temperature distribution within the DOM subdomains and perform the upwind calculation from DOM boundaries for the angular components along the wind direction. When the DOM calculations reach the contact interfaces between DOM and MC subdomains, the phonon deviational intensity calculated by DOM is converted into the property of the energy packet to be emitted (see subsubsection 2.2.2). The energy packets are then emitted one by one in MC subdomains from the contact interface during which the intrinsic and interface scatterings occur with the detailed implementations introduced in Ref. [47]. The energy packets are tracked until they

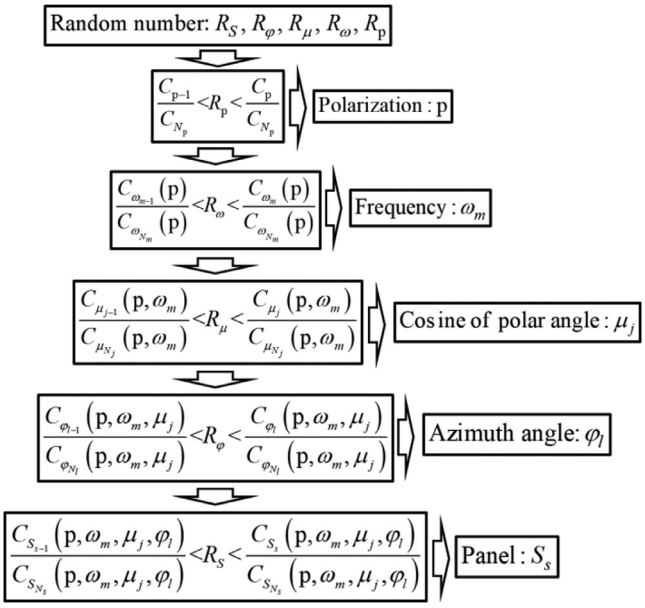


**Fig. 2.** Flow chart for delivering information from DOM to MC.

encounter the contact interface, or the total number of the scattering events reach the prescribed values. The contributions of the energy packets to the local phonon deviational intensities at the contact interface are calculated (see subsubsection 2.2.3). Then repeat the DOM simulation along the reverse direction from the contact interface towards the DOM boundaries for the remaining angular components, calculate the temperature within the DOM subdomain, and replace the pseudo-equilibrium temperature with the newest one for the next iteration. The relative error of the heat flux or the temperature between two contiguous iterations is utilized to compare with the error tolerance to determine whether to output the results and end the simulation.

In the practical simulation, due to the fluctuating nature of MC method, the relative error of two contiguous iterations may not converge to the prescribed tolerance value. Therefore, an appropriate maximum iteration number is set as the condition of ending the iteration process in this work. Besides, since the further increase of the particle number has little impact on the computational time but strongly affects the accuracy after a sufficiently accurate result reached in the DOM subdomain, the simulation is

divided into two stages to efficiently obtain the required number of the energy packets in the MC subdomain for a target error tolerance, as shown in Fig. 8. The iterations are first performed with a small number of energy packets of MC, the value of which is determined through a try calculation. Once a relatively accurate result is reached, the accuracy will be further improved by the increase of the number of energy packets of MC until the target error tolerance is reached.

*2.2.2. Information exchanging algorithm (I): DOM to MC*

In this part, our goal is to transform the information at the contact interface from the form of the prescribed phonon deviational intensity on the DOM side to the unknown particle properties to be utilized on the MC side. The main idea is to ensure the "detailed energy conservation" in the phase element $\mathrm{d}\Omega\mathrm{d}\omega\mathrm{d}S$ at each phonon polarization p by generating the properties of the MC particles emitted from the contact interface according to the local cumulative distributions in a random manner. Here, $S$ denotes the panel on the contact interface.

After obtaining the phonon intensity by DOM, the contact interface will emit energy packets into the MC side as the heat source, whose heat flux is expressed by:

$$q = \sum_{\mathrm{p}} \int_S \int_\omega \int_\Omega I^{\mathrm{d}} \mathbf{m} \cdot \mathbf{n} \mathrm{d}\Omega \mathrm{d}\omega \mathrm{d}S, \tag{14}$$

where $\mathbf{m}=\mathbf{v}_{\mathrm{g}}/v_{\mathrm{g}}$, $\mathbf{n}$ is the unit vector normal to the contact interface pointing into the MC side. Since $\mathbf{m}\cdot\mathbf{n}$ is only dependent on the polar and azimuth angles ($\theta$ and $\varphi$) of the group velocity, noting that $\mathbf{m}\cdot\mathbf{n} = \Psi(\theta)\Phi(\varphi)$ and $\mathrm{d}\Omega = \sin\theta \mathrm{d}\theta\mathrm{d}\varphi$, Eq. (14) can be rearranged as:

$$q = \sum_{\mathrm{p}} \int_S \int_\omega \int_\varphi \int_\theta I^{\mathrm{d}} \Psi(\theta)\Phi(\varphi)\sin\theta \mathrm{d}\omega\mathrm{d}\theta\mathrm{d}\varphi\mathrm{d}S. \tag{15}$$

Eq. (15) is further reduced to a summation form as below by performing Gauss Legendre quadrature in angular and frequency domains [48]:

$$q = \sum_{s,l,j,m,\mathrm{p}} I^{\mathrm{d}}\left(\mathrm{p}, \omega_m, \mu_j, \varphi_l, S_s\right)\Psi\left(\mu_j\right)\Phi(\varphi_l)\varpi_m w_j \xi_l \zeta_s, \tag{16}$$

where the weights of $\omega$, $\mu$, $\varphi$, and $S$are represented by $\varpi_m$, $w_j$, $\xi_l$, and $\zeta_s$. For 1D systems, $\Psi(\mu_j)=\mu_j$, $\Phi(\varphi_l)=2\pi$, and $\zeta_s=1$, while for 2D systems, $\Psi(\mu_j)=\sqrt{1-\mu_j^2}$ and $\Phi(\varphi_l)=\sin\varphi_l$. Set $N_s$, $N_l$, $N_j$, and $N_m$ as the maximum number of indexes of $S$, $\varphi$, $\mu$, and $\omega$ in Eq. (16), and let $N_{\mathrm{p}}$ denote the total number of polarizations. In particular, $N_l = N_s = 1$ for 1D systems. The following cumulative distributions over all phase elements at contact interface are adopted to calculate the properties of emitted energy packets in MC

$$C_{S_s}\left(\mathrm{p}, \omega_m, \mu_j, \varphi_l\right) = \sum_{i_s=1}^{s} I^{\mathrm{d}}\left(\mathrm{p}, \omega_m, \mu_j, \varphi_l, S_{i_s}\right)\zeta_{i_s}, \tag{17}$$

$$C_{\varphi_l}\left(\mathrm{p}, \omega_m, \mu_j\right) = \sum_{i_l=1}^{l} C_{S_{N_s}}\left(\mathrm{p}, \omega_m, \mu_j, \varphi_{i_l}\right)\Phi\left(\varphi_{i_l}\right)\xi_{i_l}, \tag{18}$$

$$C_{\mu_j}(\mathrm{p}, \omega_m) = \sum_{i_j=1}^{j} C_{\varphi_{N_l}}\left(\mathrm{p}, \omega_m, \mu_{i_j}\right)\Psi\left(\mu_{i_j}\right)w_{i_j}, \tag{19}$$

$$C_{\omega_m}(\mathrm{p}) = \sum_{i_m=1}^{m} C_{\mu_{N_j}}\left(\mathrm{p}, \omega_{i_m}\right)\varpi_{i_m}, \tag{20}$$

$$C_{\mathrm{p}} = \sum_{i_{\mathrm{p}}=1}^{\mathrm{p}} C_{\omega_{N_m}}(i_{\mathrm{p}}), \tag{21}$$

Specifically, for each emitted energy packets in MC, five numbers are first generated between 0 and 1 randomly, namely $R_S$, $R_\varphi$, $R_\mu$, $R_\omega$, and $R_{\mathrm{p}}$. Then the properties of this energy packet to be emitted is determined by comparing the random number with the corresponding normalized distribution on by one. For example, first compare $R_{\mathrm{p}}$ with the normalized distribution of polarization p, if $\frac{C_{\mathrm{p}-1}}{C_{N_{\mathrm{p}}}} < R_{\mathrm{p}} < \frac{C_{\mathrm{p}}}{C_{N_{\mathrm{p}}}}$, the polarization of the emitted energy packet is assigned to p; then compare $R_\omega$ with the normalized distribution of frequency $\omega$, if $\frac{C_{\omega_{m-1}}(\mathrm{p})}{C_{\omega_{N_m}}(\mathrm{p})} < R_\omega < \frac{C_{\omega_m}(\mathrm{p})}{C_{\omega_{N_m}}(\mathrm{p})}$, the frequency of the emitted energy packet is assigned to $\omega_{\mathrm{m}}$. The remaining properties of the energy packet can be determined similarly. In this way, all necessary information for the MC simulation will be obtained, indicating that the information on the DOM side is successfully delivered to the MC side.

*2.2.3. Information exchanging algorithm (II): MC to DOM*

In this part, our goal is to transform the information at the contact interface from the form of the prescribed particle properties on the MC side to the unknown phonon deviational intensity to be utilized on the DOM side. Because this is only a particle-to-continuum conversion, the algorithm here is simply performing the local statistics, i.e., to collect and count the number of the particles reaching the contact interface in each phase element.

Since the energy is conserved at the contact interface, the heat fluxes expressed by MC and DOM are equal to each other, namely

$$\sum_{i_0=1}^{N} \eta_\mu \sigma_{i_0} \varepsilon_{\mathrm{eff}} = \sum_{s,l,j,m,\mathrm{p}} I^{\mathrm{d}}\left(\mathrm{p}, \omega_m, \mu_j, \varphi_l, S_s\right)\Psi\left(\mu_j\right)\Phi(\varphi_l)\varpi_m w_j \xi_l \zeta_s. \tag{22}$$

where we have used the heat flux formulations Eq. (16) on the DOM side and Eq. (13) on the MC side. Eq. (22) is indeed a cumulative version of "detailed energy conservation", namely

$$\sum_{i_0=1}^{N_0} \eta \sigma_{i_0} \varepsilon_{\mathrm{eff}} = I^{\mathrm{d}}\left(\mathrm{p}, \omega_m, \mu_j, \varphi_l, S_s\right)\Psi\left(\mu_j\right)\Phi(\varphi_l)\varpi_m w_j \xi_l \zeta_s. \tag{23}$$

where $N_0$ represents the total number of energy packets with polarization p and frequency $\omega_m$ and other properties around the discrete values $S_s$, $\varphi_l$, and $\mu_j$.

To determine the particles contributed to Eq. (23), it is required to give the precise definition of the neighborhood of these discrete points for further statistical operation. Considering the cumulative distributions of $S$, $\varphi$, and $\mu$ in DOM

$$C_s = \sum_{i_0=1}^{s} \zeta_{i_0},\ C_l = \sum_{i_0=1}^{l} \xi_{i_0},\ C_j = \sum_{i_0=1}^{j} w_{i_0}, \tag{24}$$

for an energy packet at the contact interface from the MC side, if its property $S_0$, $\varphi_0$, and $\mu_0$ satisfies

$$C_{s-1} < S_0 < C_s,\ C_{l-1} < \varphi_0 < C_l,\ C_{j-1} < \mu_0 < C_j, \tag{25}$$

the properties of this energy packet are assigned to $S_s$, $\varphi_l$, and $\mu_j$ on the DOM side, respectively. According to Eq. (23), the phonon intensity across the contact interface from the MC side to the DOM side can be obtained by

$$\psi\left(\mathrm{p}, \omega_m, \mu_j, \varphi_l, S_s\right) = \sum_{i_0=1}^{N_0} \frac{\eta \sigma_{i_0} \varepsilon_{\mathrm{eff}}}{\Psi\left(\mu_j\right)\Phi(\varphi_l)\varpi_m w_j \xi_l \zeta_s}, \tag{26}$$

## 3. Verifications: Cross-plane Phonon Transport through Thin Film

In this section, the proposed hybrid MC-DOM model is verified by considering the cross-plane phonon transport through

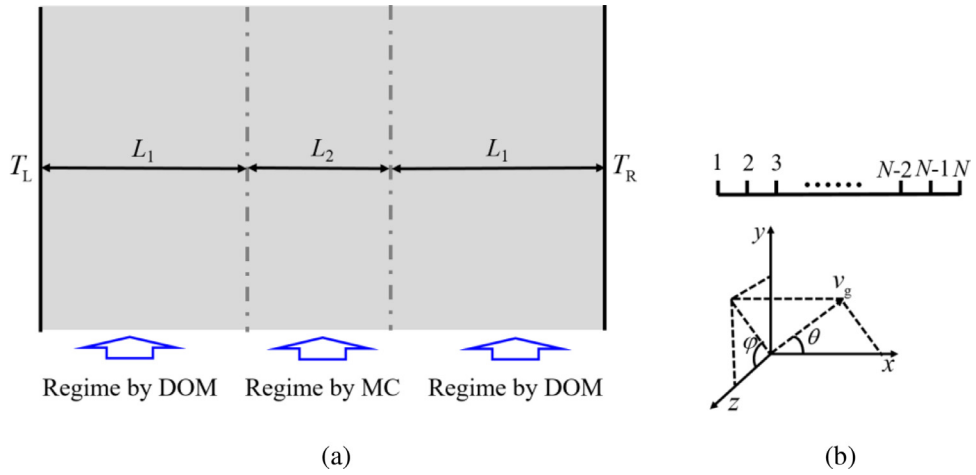


**Fig. 3.** Cross-plane phonon transport through the single-layer thin film: (a) the physical model; (b) the spatial discretization diagram of the DOM subdomain and the corresponding coordinate system. The dash lines denote the contact interface between the DOM and MC subdomains.

single/double-layer thin films and comparing the results of hybrid model with the accurate ones from DOM algorithm [31,68]. The 1D transport is chosen for verification because of their simplicity to obtain the accurate results by DOM. In particular, the efficiency of the hybrid MC-DOM solver and pure MC solvers are compared under the same error tolerance of temperature and heat flux regarding the former case.

### 3.1. Single-layer thin film

The steady-state cross-plane phonon transport through the single-layer thin film at steady state is illustrated in Fig. 3. The intensity-based BTE for 1D system here is reduced as below based on Eq. (5)

$$v_g(\omega, \mathrm{p})\mu \frac{\partial I^{\mathrm{d}}}{\partial x} = -\frac{I^{\mathrm{d}} - \left(I^{\mathrm{eq}}_{\mathrm{pse}}\left(T^{\mathrm{eq}}_{\mathrm{pse}}\right) - I^{\mathrm{eq}}_{\mathrm{ref}}\left(T^{\mathrm{eq}}_{\mathrm{ref}}\right)\right)}{\tau(\omega, \mathrm{p}, T)}, \tag{27}$$

where the reference equilibrium temperature is taken as a constant. Three materials are simulated, namely Si, Al, and Ge, with properties referred to Section 2.

The left and right isothermal boundaries are fixed at $T_L = 303$ K and $T_R = 297$ K with a constant reference equilibrium temperature $T^{\mathrm{eq}}_{\mathrm{ref}} = 300$ K. The total thicknesses $L = 2L_1 + L_2$ of thin films are set to 10 nm, 30 nm, ..., 90 nm, 110 nm, 210 nm, ..., 510 nm, with the corresponding thicknesses $L_1$ set to 2 nm, 10 nm, 20nm, ..., 50 nm, 100 nm, 150 nm, ..., 250 nm in the DOM subdomains, respectively. The spatial step $\Delta x$ in DOM is fixed at 0.01 nm and the angular domain is discretized into 32 Gaussian points. The total numbers of energy packets in MC are set to $10^7$. The maximum numbers of iterations are set to 300 for the $L < 90$ nm and 600 for the others.

Fig. 4 gives the results of temperature and heat flux distributions, as well as the cross-plane thermal conductivities simulated by the present hybrid method. The effective cross-plane thermal conductivity is defined by the phenomenological Fourier's law, $\lambda = -qL/(T_R - T_L)$ with the heat flux $q$ across the film. All the results agree well with those calculated by DOM, which verifies the present hybrid method for the case of the steady-state cross-plane phonon transport through the single-layer thin film.

### 3.2. Double-layer thin film

The steady-state cross-plane phonon transport through a double-layer thin film at a steady state is illustrated in Fig. 5 (a). The intensity-based BTE of the present case is also Eq. (27) with a constant reference equilibrium temperature. The films are of Al/Si or Ge/Si with properties in Section 2. The spectral diffuse mismatch model is adopted to describe the phonon behavior at the interface [47].

The left and right isothermal boundaries are set to $T_L = 303$ K and $T_R = 297$ K with a constant reference equilibrium temperature $T^{\mathrm{eq}}_{\mathrm{ref}} = 300$ K. The total thicknesses $L = 2L_1 + 2L_2$ are set to 20 nm, 60 nm, ..., 220 nm, with the corresponding thicknesses $L_1$ set to 7 nm, 25 nm, 45 nm, ..., 105 nm in the DOM subdomain. The spatial step $\Delta x$ of DOM is fixed at 0.01 nm and the angular domain is discretized into 48 Gaussian points. The total numbers of energy packets in MC are set to $10^7$. The maximum numbers of iterations are set to 500 for the $L < 10$ nm and 800 for the others.

Figs. 6 and 7 shows the comparisons of the temperature distribution and the thermal boundary conductance between the present hybrid method and DOM. Here the thermal boundary conductance is defined by $G = q/\Delta T$, where $\Delta T$ denotes the temperature jump at the interface. The above results agree well with each other, verifying the present hybrid method for the case of steady-state cross-plane phonon transport through the double-layer thin film.

### 3.3. Discussion on the efficiency

The computational efficiency of the present hybrid MC-DOM is compared with that of pure MC method in this subsection by considering the single-layer case in Section 3.1. The flow chart of the two methods to be compared here is illustrated in Fig. 8. The total thicknesses for the films simulated by two methods are set equal. Due to the lack of the analytical solution for the present case, the heat flux obtained by the DOM is used as the accurate result after a number of iterations to reach the sufficient accuracy. The comparison of computational efficiency between the hybrid method and pure MC method is denoted by the total computational time under prescribed target error tolerance between the calculated value and the exact value.

Single layer made of Si is considered in this subsection. The thickness is fixed at 100 nm with $T_L = 301$ K and $T_R = 299$ K. For the Monte Carlo method, the initial number of the energy packets is set to $N_1 = 2 \times 10^6$. For the hybrid method, the thicknesses of the DOM and MC subdomains are fixed at $L_1 = 45$ nm and $L_2 = 10$ nm, respectively. The spatial and angular steps in DOM's discretization are set to 0.01 nm and 32 for a better balance of accuracy and efficiency. Since the thickness of the MC subdomain in the hybrid method is one-tenth of the total thickness, the initial number of the energy packets is set to $N_2 = 1 \times 10^5$ and the num-

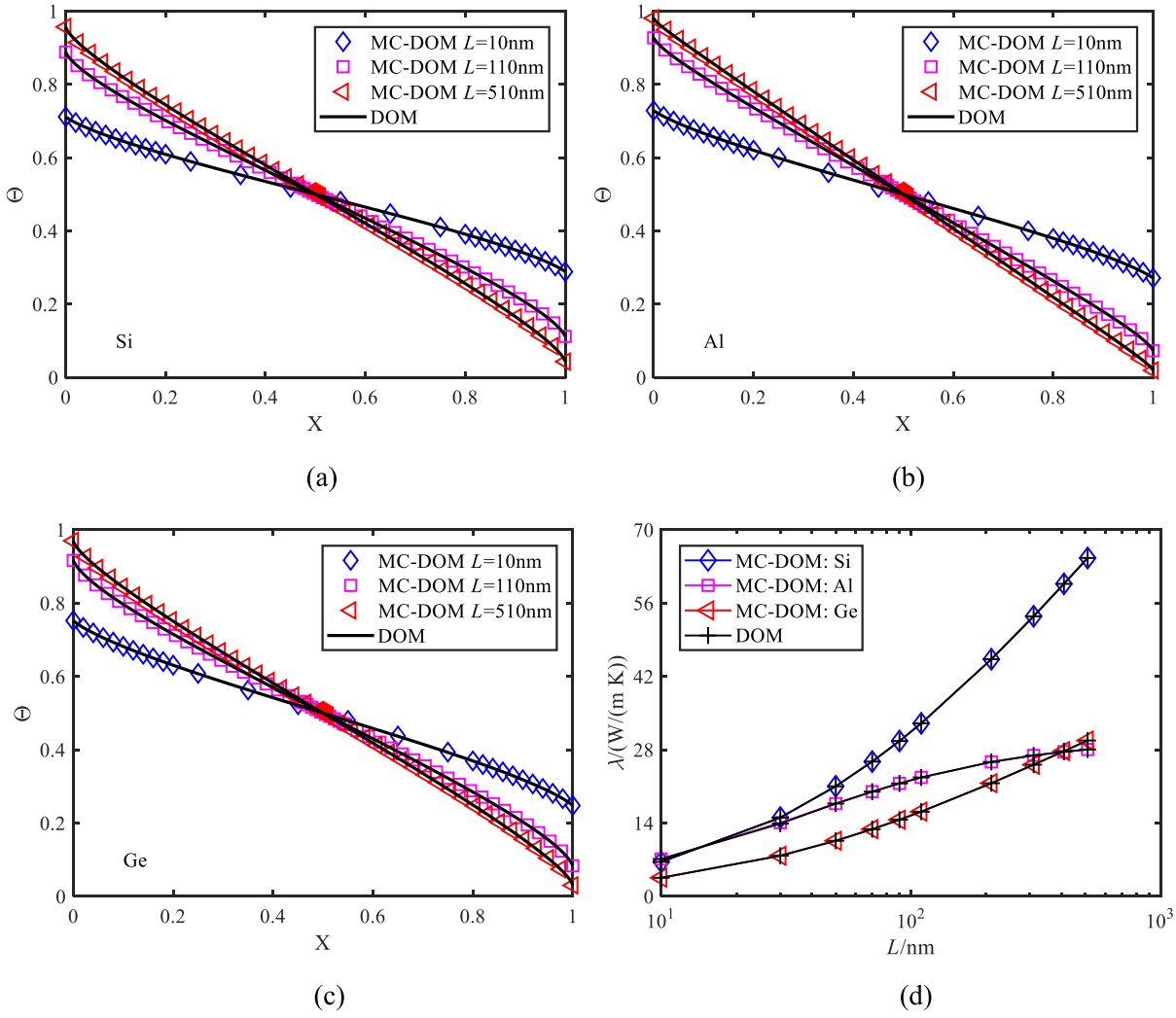


**Fig. 4.** The dimensionless temperature distribution and the cross-plane thermal conductivity: (a)-(c) the dimensionless temperature distribution for Si, Al and Ge; (d) the cross-plane thermal conductivities for three materials.

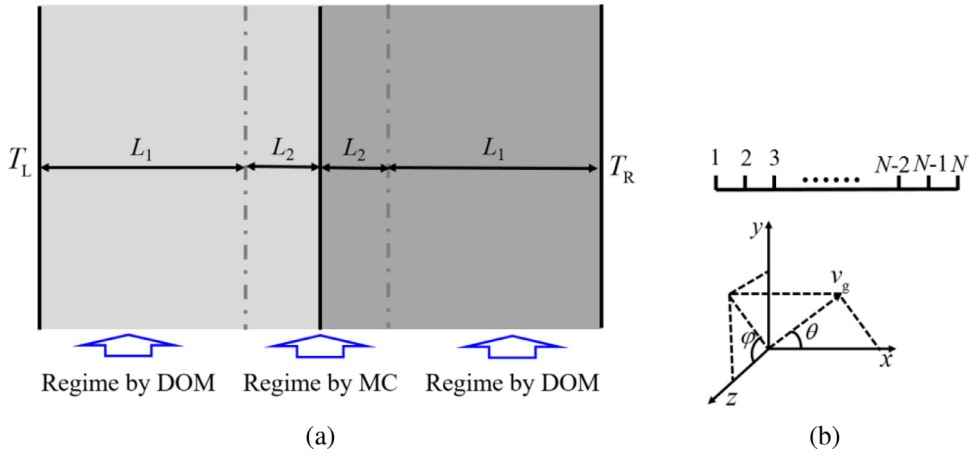


**Fig. 5.** Cross-plane phonon transport through the double-layer thin film: (a) the physical model; (b) the spatial discretization diagram of the DOM subdomain and the corresponding coordinate system. The dash lines denote the contact interface between the DOM and MC subdomains.

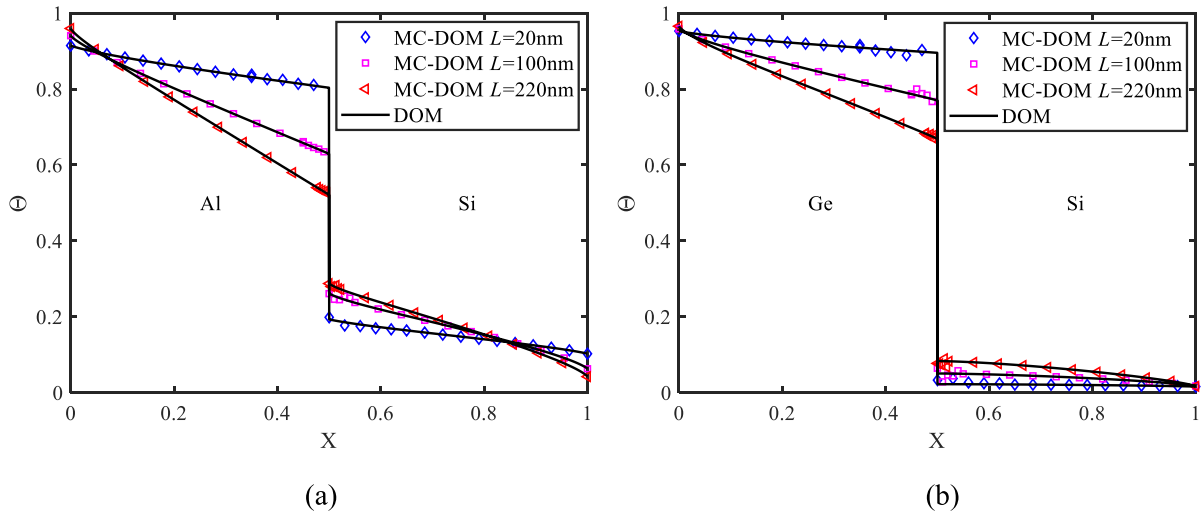


**Fig. 6.** The dimensionless temperature distribution: (a) Al/Si film; (b) Ge/Si film.

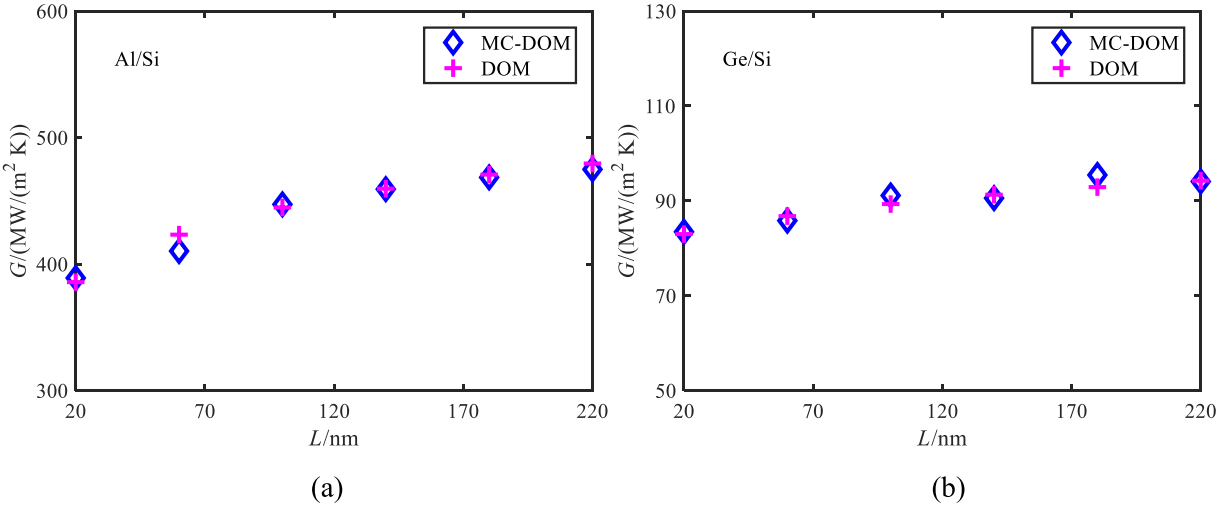


**Fig. 7.** The thermal boundary conductance at various total thicknesses: (a) Al/Si film; (b) Ge/Si film.

ber step in the second stage of iterations is set to $N_3 = 2 \times 10^5$. From a try calculation, the accurate results can be obtained after about 60 iterations.

Since the rate of convergence shows distinctions between the temperature and heat flux, the efficiency comparison is performed separately under two types of convergence criterions corresponding to the relative errors defined by the above two variables, respectively. Specifically, the whole film is uniformly divided into 40 grids and the relative errors are calculated at the center of these grids. The relative errors based on the temperature and the heat flux are defined as $\sigma_T = \frac{1}{40}\sum_{a=1}^{40}|T_a - T_a^C|/T_a^C$ and $\sigma_q = \frac{1}{40}\sum_{a=1}^{40}|q_a - q_a^C|/q_a^C$, where $a$ is the index of the unit, $T_a$ and $q_a$ the temperature and the heat flux obtained by MC and the hybrid method, $T_a^C$ and $q_a^C$ the exact values of the temperature. The target relative errors are set to $1.5 \times 10^{-6}$ and $1 \times 10^{-4}$ for the temperature and the heat flux respectively.

Table 2 presents the results of the required computing times for the target error tolerance by MC and the hybrid method. It is found that for the temperature calculation, the computing time of the hybrid method is about one in 136 to that of MC, indicating that the computational efficiency of the former is much higher than the latter, while for the calculation of the heat flux, the computational efficiencies of both methods are comparable. It is inferred that the huge difference between the results for the temperature and the heat flux may be ascribed to the different error tolerances set to temperature and heat flux, which indicates the high performance of our hybrid method when a high-precision result is required. It is expected that once the system scale is comparable to microns, the required number of energy packets in MC will be quite large to satisfy even a less stringent demand on the target accuracy, which makes our hybrid method appealing and useful.

Nevertheless, the relative performance among the modeling methods (e.g., hybrid BTE-based mesoscopic methods and hybrid BTE-diffusion methods with either particle-based or discretization-based BTE solvers) is strongly influenced by several factors, including the physical requirements (e.g., characteristic system length and phonon mean free path) and numerical issues (e.g., interfacial complexity and error tolerance). Regarding the hierarchy of the methods on their applicability of characteristic length scale of the simulated system, it remains an open question whether the "op-

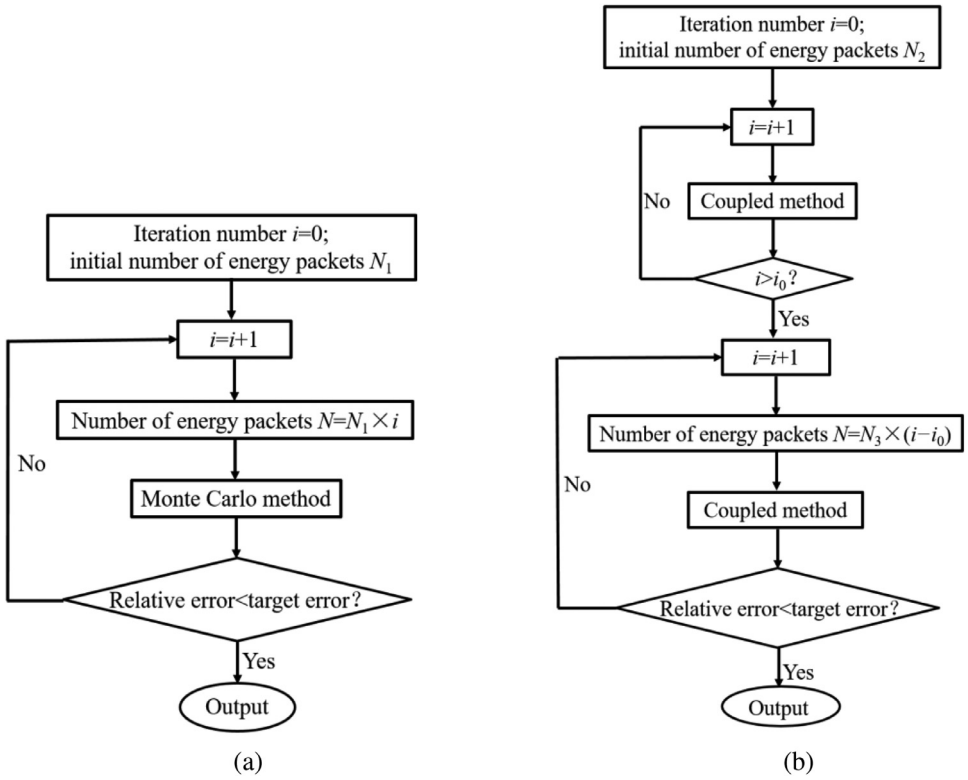


**Fig. 8.** The flow chart for the comparisons of the computational efficiencies of two methods: (a) pure MC method; (b) the hybrid MC-DOM, where $i_0$ denotes the minimum number of iterations for DOM subdomains to reach an accuracy approximated to the target one, which is required to start the second stage of iterations.

**Table 2**
The comparison for the computing times of Monte Carlo method and the hybrid method.

| Method | Computing time (for temperature) | Computing time (for heat flux) |
|---|---|---|
| Pure MC | 12674 s | 111 s |
| Hybrid method | 93 s | 110 s |

timized scale window" exists for the hybrid MC-DOM model, in which the scale is small enough for the macroscopic method to be invalid and large enough for the computational costs of the stochastic method (required to suppress the statistical variance to satisfy the prescribed error tolerance) to be prohibitive. Detailed comparisons of the accuracy and efficiency performance between our mesoscopic hybrid MC-DOM model and other models (e.g., MC, DOM, hybrid BTE-diffusion method) are required but far beyond our concern in this work, and thus will be left to further studies.

## 4. Applications: In-plane Phonon Transport through Thin Film

In this section, the hybrid MC-DOM model is applied to the in-plane phonon transport through single/double-layer thin films. Specifically, the 2D in-plane transport through a single layer thin film is first verified by comparing the results with the accurate solution of phonon BTE. Then the hybrid MC-DOM model is adopted to study the influence of rectangular rough interfaces on the in-plane phonon thermal conductivity of the double-layer thin film, which shows the superiority of our novel hybrid method for those mesoscopic systems with complex interfaces.

### 4.1. Single-layer thin film

The steady-state in-plane phonon transport through the single-layer thin film is simulated by the present hybrid method, as shown in Fig. 9(a). The constant external temperature gradient is applied at $x$ direction along the film. The intensity-based BTE for the present 2D system is reduced as below based on Eq. (5):

$$v_{g,x}\frac{\partial I^{d}}{\partial x}+v_{g,y}\frac{\partial I^{d}}{\partial y}=\frac{\left(I_{pse}^{eq}\left(T_{pse}^{eq}\right)-I_{ref}^{eq}\left(T_{ref}^{eq}\right)\right)-I^{d}}{\tau\left(\omega,\mathrm{p},T\right)}+Q_{V}, \tag{28}$$

where $Q_V=-\mathbf{v}_g\cdot\nabla I_{ref}^{eq}(T_{ref}^{eq}(x))$ is the volume heat source by introducing the reference equilibrium temperature varying with $x$ linearly, which represents the external temperature gradient and paves the way to implement the periodic heat flux boundary condition [51,66], $v_{g,x}=v_g\mu$ and $v_{g,y}=v_g\sin\varphi\sqrt{1-\mu^2}$.

$$v_{g}\mu\frac{\partial I^{d}}{\partial x}+v_{g}\sin\varphi\sqrt{1-\mu^{2}}\frac{\partial I^{d}}{\partial y}=\frac{\left(I_{pse}^{eq}\left(T_{pse}^{eq}\right)-I_{ref}^{eq}\left(T_{ref}^{eq}\right)\right)-I^{d}}{\tau\left(\omega,\mathrm{p},T\right)}+Q_{V}. \tag{29}$$

The single layers made of three materials are simulated in this subsection, namely Si, Al, and Ge, whose properties are referred to Section 2.

The equilibrium temperatures at the left and right periodic heat flux boundaries are set to $T_L=301$ K and $T_R=299$ K, respectively. The thicknesses of the films at $x$ direction are $L_x=1$ nm and the external temperature gradients are calculated by $\nabla T=(T_R-T_L)/L_x$, with the reference equilibrium temperatures set to $T_{ref}^{eq}(x=0)=301$ K and $T_{ref}^{eq}(x=L_x)=299$ K. The total thicknesses $L=2L_1+L_2$ are set to 20 nm, 30 nm, ..., 100 nm and the thicknesses $L_1$ are set to 7 nm for $L=20$ nm and 10 nm for the other cases in the DOM subdomains. The spatial step $\Delta x$ in DOM is fixed at 0.25 nm and

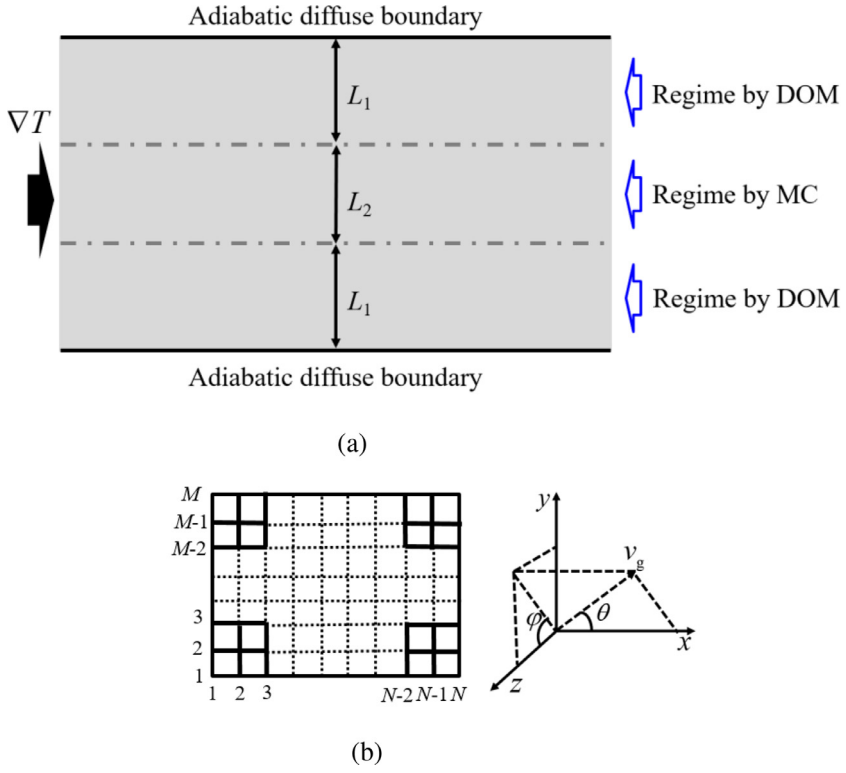


**Fig. 9.** In-plane phonon transport through the single-layer thin film: (a) the physical model; (b) the spatial discretization diagram of the DOM subdomain and the corresponding coordinate system. The dash lines denote the contact interface between the DOM and MC subdomains.

the numbers of discrete points for $\mu$ and $\varphi$ are set to 32 and 200 respectively, while the numbers of the energy packets in MC are set to 2, 3, ..., 10 ($\times 10^7$). The maximum numbers of iterations are set to 600.

The heat flux distributions and in-plane thermal conductivities obtained by the present hybrid method are compared with the analytical solution in Fig. 10. The effective in-plane thermal conductivity is also obtained based on the phenomenological Fourier's law $\lambda = -\int_0^L q_x dy/\nabla T$. Good agreements of all the comparisons show that the present hybrid method has been verified for the case of the steady-state in-plane phonon transport through the single-layer thin film.

### 4.2. Double-layer thin film with a rough interface

Finally, the hybrid method is applied to study of the in-plane phonon transport through a double-layer thin film with a periodic rectangular rough interface, as shown in Fig. 11. The period and height of the roughness are $4L_3$ and $h_0$. The upper and lower boundaries of the films are adiabatic boundaries with a completely diffuse scattering. The left and right boundaries are taken as the periodic heat flux boundaries as before. Two material pairs are considered here, namely 1(Ge)/2(Si) and 1(Al)/2(Si), with same properties as mentioned before, and the volume ratio of the two materials in each film are fixed at 1. The external temperature gradient is calculated by $\nabla T = (T_R - T_L)/4L_3$, where $T_L = 301$ K and $T_R = 299$ K are the temperatures at the left and right periodic heat flux boundaries. The total thicknesses of all films are fixed at $L = 40$ nm. The spatial steps along $x$ and $y$ directions as 1 nm. The numbers of the energy packets in the region of MC are set to $1.6 \times 10^7$. The maximum numbers of the iterations for the hybrid method are set to 60.

Three groups of cases are considered here to investigate the influence of the interfacial roughness to the in-plane thermal conductivity of the double-layer thin film. In the first group, the heights of the rough interface $h_0$ are fixed at 10 nm, the lengths $L_3$ are set to 2.5 nm, 4 nm, 5.5 nm, 7 nm, 8.5 nm, and 10 nm, and the thicknesses of the DOM subdomains $L_1$ are fixed at 10 nm. In the second group, the lengths $L_3$ are fixed at 4 nm, the heights of the roughness $h_0$ set to 8 nm, 12 nm, 16 nm, 20 nm, 24 nm, and 28 nm, and the thicknesses of the DOM subdomains set to 10 nm, 10 nm, 8 nm, 6 nm, 4 nm, and 3 nm. In the third group, the ratios of height and period are fixed at 1, the heights of the roughness $h_0$ set to 8 nm, 12 nm, 16 nm, 20 nm, 24 nm, and 28 nm, and the thicknesses of the DOM subdomains set to 10 nm, 10 nm, 8 nm, 6 nm, 4 nm, and 3 nm.

The effective in-plane thermal conductivity is calculated by $\lambda = -\int_0^L q_x dy/\nabla T$. As shown in Fig. 12, the in-plane thermal conductivity increases with the increased period of the rough interface for the fixed height, while decreasing with the increased height of the rough interface and the increased height and period with a fixed ratio. The physical mechanism for the previous results is analyzed as below. As shown in Fig. 13, among the interfaces with the roughness, two kinds of interfaces can be recognized, i.e., the ones parallel to and the others perpendicular to the direction of the heat flux, which are related to the period and the height of the roughness respectively. Due to the reflection of phonons by the interface, which makes the non-equilibrium effect at the interface perpendicular to the heat flux is larger than that at the other kind of interface and thus the larger thermal resistance along the previous interface, which makes the scattering intensity between phonons and the interface perpendicular to the heat flux impact more greatly on the in-plane thermal conductivity. Based on the results above, the thermal resistance of a double-layer thin film can be regulated by adjusting the number of or the distance between the two kinds of interfaces, especially when the total thickness of the film becomes comparable to the phonon mean free path.

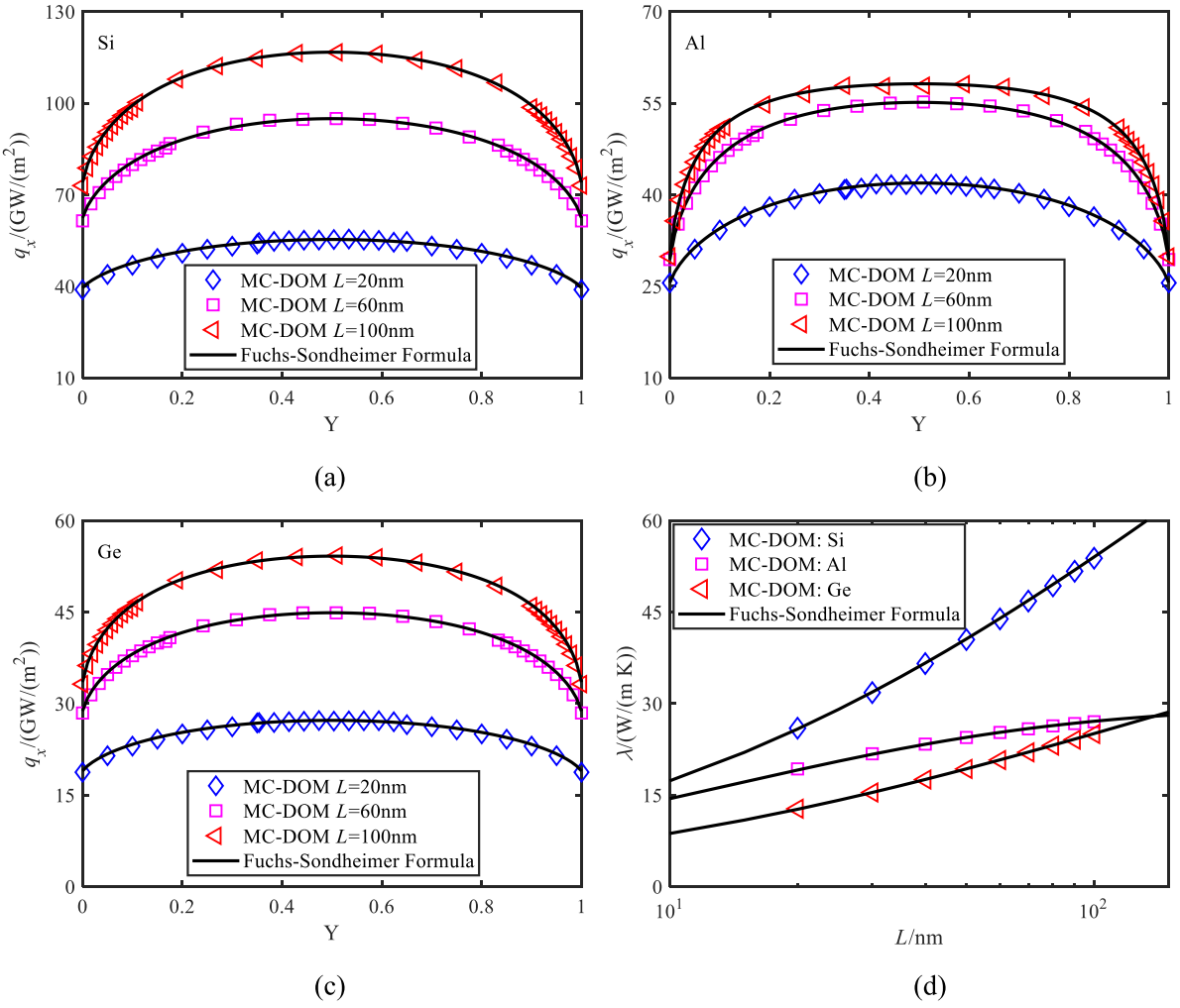


**Fig. 10.** The heat flux distribution and the in-plane thermal conductivity: (a) the heat flux distribution for Si; (b) the heat flux distribution for Al; (c) the heat flux distribution for Ge; (d) the in-plane thermal conductivities for three materials.

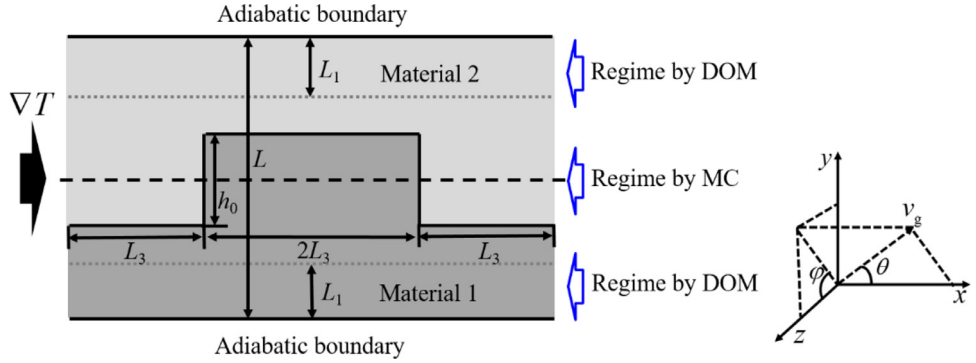


**Fig. 11.** The physical model for in-plane phonon transport through the double-layer thin film with the periodic rectangular rough interface. The dash lines denote the contact interface between the DOM and MC subdomains.

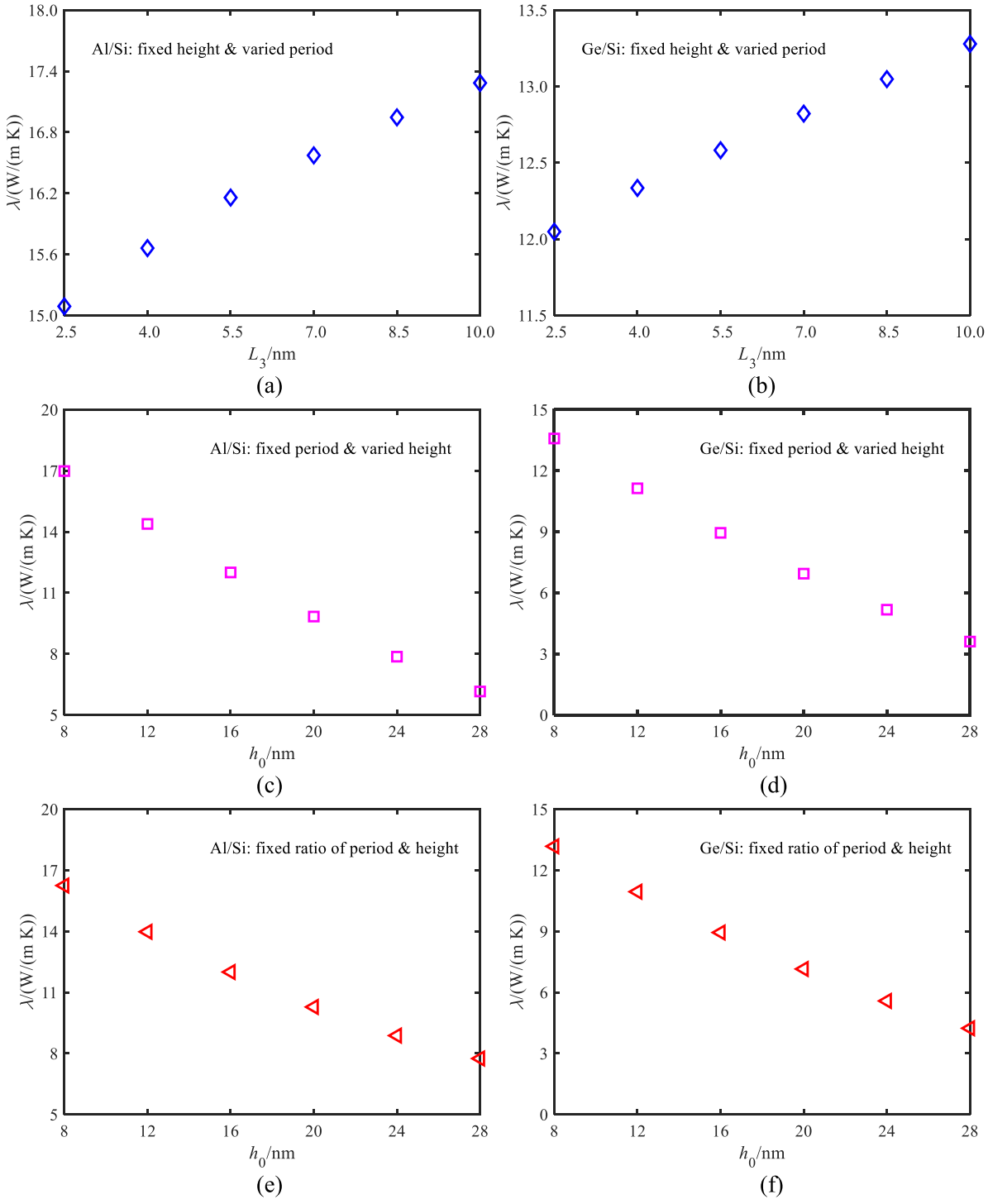


**Fig. 12.** The in-plane thermal conductivity of the double-layer thin film with the periodic rectangular rough interface: (a) the fixed height and varied period for the film made of Al/Si; (b) the fixed height and varied period for the film made of Ge/Si; (c) the fixed period and varied height for the film made of Al/Si; (d) the fixed period and varied height for the film made of Ge/Si; (e) the fixed ratio of the height and period for the film made of Al/Si; (f) the fixed ratio of the height and period for the film made of Ge/Si.

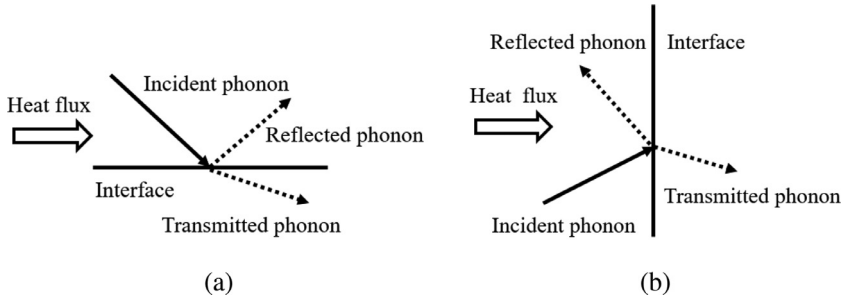


**Fig. 13.** The diagram for phonons scattered at interfaces in different placement directions: (a) the interface scattering phonons parallel to the heat flux; (b) the interface scattering phonons perpendicular to the heat flux.

## 5. Conclusions

In summary, via developing the numerical algorithm to exchange the information between Monte Carlo method (MC) and discrete ordinates method (DOM) subdomains, a hybrid MC-DOM model for steady-state phonon transport is proposed in the present work. The hybrid method is first verified by simulating the cross-plane phonon transport through the single/double-layer thin films. If high-precision results are required, the computational efficiency is substantially improved compared with pure MC for the temperature calculation. The in-plane phonon transport through the single/double-layer thin film with the periodic rectangular rough interface is simulated by the hybrid method. The results show that the in-plane thermal conductivity of thin film is impacted more greatly by the change of height of the roughness, corresponding to those roughness interfaces perpendicular to heat flux. The present work promotes the mesoscopic numerical tools, and the results on impact factors of the in-plane thermal conductivity provide the insights to the optimized thermal designs in micro/nanosystems.

## Declaration of Competing Interest

The authors declare the following financial interests/personal relationships which may be considered as potential competing interests.

## CRediT authorship contribution statement

**Xin Ran:** Investigation, Software, Writing – original draft. **Yunfan Huang:** Validation, Writing – original draft. **Moran Wang:** Conceptualization, Supervision, Writing – review & editing, Project administration.

## Data Availability

No data was used for the research described in the article.

## Acknowledgements

This work is financially supported by NSF of China (No. 12272207) and the Tsinghua University Initiative Scientific Research Program. Our simulations are run on the “Explorer 100” cluster of Tsinghua National Laboratory for Information Science and Technology.

## Appendix A. Formation of Intensity-based deviational DOM

### A.1. One-dimensional case

For 1D cases, the spatial discretization of the DOM subdomain is illustrated in Fig. 3 (b). Eq. (27) is discretized using the semi-implicit upwind scheme [33]

$$m\left(I^{\mathrm{d}}_{i,j,m,\mathrm{p}}-I^{\mathrm{d}}_{i-\sigma_\mu,j,m,\mathrm{p}}\right)=-\frac{I^{\mathrm{d}}_{i,j,m,\mathrm{p}}-\left(I^{\mathrm{eq}}_{\mathrm{pse},i,j,m,\mathrm{p}}-I^{\mathrm{eq}}_{\mathrm{ref},m,\mathrm{p}}\right)}{\tau\left(\omega_m,\mathrm{p},T\right)},\tag{30}$$

where $m=\frac{v_{\mathrm{g}}(\omega_m,\mathrm{p})|\mu_j|}{\Delta x}$ and $\sigma_\mu=\mathrm{sign}(\mu_j)$. Eq. (30) could be re-arranged to the following form for iteration

$$I^{\mathrm{d}}_{i,j,m,\mathrm{p}}=\frac{mI^{\mathrm{d}}_{i-\sigma_\mu,j,m,\mathrm{p}}+\left(I^{\mathrm{eq}}_{\mathrm{pse},i,j,m,\mathrm{p}}-I^{\mathrm{eq}}_{\mathrm{ref},m,\mathrm{p}}\right)/\tau\left(\omega_m,\mathrm{p},T\right)}{m+1/\tau\left(\omega_m,\mathrm{p},T\right)}.\tag{31}$$

### A.2. Two-dimensional case

Similar to the 1D cases, the semi-implicit upwind scheme is also used for the discretization of 2D phonon BTE Eq. (29)

$$\begin{aligned}m_1\left(I^{\mathrm{d}}_{i,u,j,l,m,\mathrm{p}}-I^{\mathrm{d}}_{i-\sigma_\mu,u,j,l,m,\mathrm{p}}\right)+m_2\left(I^{\mathrm{d}}_{i,u,j,l,m,\mathrm{p}}-I^{\mathrm{d}}_{i,u-\sigma_\varphi,j,l,m,\mathrm{p}}\right)\\=-\frac{I^{\mathrm{d}}_{i,u,j,l,m,\mathrm{p}}-\left(I^{\mathrm{eq}}_{\mathrm{pse},i,u,j,l,m,\mathrm{p}}-I^{\mathrm{eq}}_{\mathrm{ref},i,m,\mathrm{p}}\right)}{\tau\left(\omega_m,\mathrm{p},T\right)}+Q_V\end{aligned},\tag{32}$$

where $m_1=\frac{v_{\mathrm{g}}(\omega_m,\mathrm{p})|\mu_j|}{\Delta x}$, $m_2=\frac{v_{\mathrm{g}}(\omega_m,\mathrm{p})|\sin\varphi_l|\sqrt{1-\mu_j^2}}{\Delta y}$, $\sigma_\mu=\mathrm{sign}(\mu_j)$, and $\sigma_\varphi=\mathrm{sign}(\sin\varphi_l)$. Eq. (32) could be re-arranged to the following form for iteration

$$I^{\mathrm{d}}_{i,u,j,l,m,\mathrm{p}}=\frac{m_1I^{\mathrm{d}}_{i-\sigma_\mu,u,j,l,m,\mathrm{p}}+m_2I^{\mathrm{d}}_{i,u-\sigma_\varphi,j,l,m,\mathrm{p}}+\frac{I^{\mathrm{eq}}_{\mathrm{pse},i,u,j,l,m,\mathrm{p}}-I^{\mathrm{eq}}_{\mathrm{ref},i,m,\mathrm{p}}}{\tau\left(\omega_m,\mathrm{p},T\right)}+Q_V}{m_1+m_2+1/\tau\left(\omega_m,\mathrm{p},T\right)}.\tag{33}$$

## References

[1] A. Majumdar, Thermoelectricity in semiconductor nanostructures, Science 303 (5659) (2004) 777–778.
[2] G.J. Snyder, E.S. Toberer, Complex thermoelectric materials, Nat. Mater. 7 (2) (2008) 105–114.
[3] A.A. Maznev, J.A. Johnson, K.A. Nelson, Onset of nondiffusive phonon transport in transient thermal grating decay, Phys. Rev. B 84 (19) (2011) 195206.
[4] J.A. Johnson, et al., Direct measurement of room-temperature nondiffusive thermal transport over micron distances in a silicon membrane, Phys. Rev. Lett. 110 (2) (2013) 025901.
[5] R.B. Wilson, D.G. Cahill, Anisotropic failure of Fourier theory in time-domain thermoreflectance experiments, Nat. Commun. 5 (2014) 5075.
[6] M. Wang, N. Yang, Z.-Y. Guo, Non-Fourier heat conductions in nanomaterials, J. Appl. Phys. 110 (6) (2011) 064310.
[7] A. Majumdar, Microscale Heat Conduction in Dielectric Thin Films, J. Heat Transfer 115 (1) (1993) 7–16.
[8] H.S. Wijesinghe, et al., Three-dimensional Hybrid Continuum-Atomistic Simulations For Multiscale Hydrodynamics, J. Fluids Eng. 126 (5) (2004) 768–777.
[9] Wijesinghe, H.S. and N.G. Hadjiconstantinou, Discussion of hybrid atomistic-continuum methods for multiscale hydrodynamics. 2004. 2(2): p. 15.
[10] S. Chen, M. Wang, Z. Xia, Multiscale fluid mechanics and modeling, Procedia IUTAM 10 (2014) 100–114.
[11] J.M. Loy, J.Y. Murthy, D. Singh, A fast hybrid Fourier–Boltzmann transport equation solver for Nongray phonon transport, J. Heat Transfer 135 (1) (2013) 011008.
[12] N. Donmezer, S. Graham, A multiscale thermal modeling approach for ballistic and diffusive heat transport in two dimensional domains, Int. J. Therm. Sci. 76 (2014) 235–244.

[13] W. Cheng, A. Alkurdi, P.O. Chapuis, Coupling mesoscopic Boltzmann transport equation and macroscopic heat diffusion equation for multiscale phonon heat conduction, Nanoscale Microscale Thermophys. Eng. 24 (3-4) (2020) 150–167.
[14] H.-L. Li, Y.-C. Hua, B.-Y. Cao, A hybrid phonon Monte Carlo-diffusion method for ballistic-diffusive heat conduction in nano- and micro- structures, Int. J. Heat Mass Transfer 127 (2018) 1014–1022.
[15] N.G. Hadjiconstantinou, et al., Statistical error in particle simulations of hydrodynamic phenomena, J. Comput. Phys. 187 (1) (2003) 274–297.
[16] A. Donev, et al., On the accuracy of finite-volume schemes for fluctuating hydrodynamics, Commun. Appl. Math. Comput. Sci. 5 (2) (2010) 149–197.
[17] P. Koumoutsakos, Multiscale flow simulations using particles, Annu. Rev. Fluid Mech. 37 (1) (2005) 457–487.
[18] M.N. Guddati, S. Thirunavukkarasu, Phonon absorbing boundary conditions for molecular dynamics, J. Comput. Phys. 228 (21) (2009) 8112–8134.
[19] L. Sun, J.Y. Murthy, Molecular dynamics simulation of phonon scattering at silicon/germanium interfaces, J. Heat Transfer 132 (10) (2010) 102403.
[20] T. Feng, et al., Spectral analysis of nonequilibrium molecular dynamics: Spectral phonon temperature and local nonequilibrium in thin films and across interfaces, Phys. Rev. B 95 (19) (2017) 195202.
[21] H. Xie, M. Hu, H. Bao, Thermal conductivity of silicene from first-principles, Appl. Phys. Lett. 104 (13) (2014) 131906.
[22] C. Jacoboni, L. Reggiani, The Monte Carlo method for the solution of charge transport in semiconductors with applications to covalent materials, Rev. Mod. Phys. 55 (3) (1983) 645–705.
[23] J.-P.M. Peraud, C.D. Landon, N.G. Hadjiconstantinou, Monte Carlo methods for solving the Boltzmann transport equation, Annu. Rev. Heat Transfer 17 (N/A) (2014) 205–265.
[24] A. Nabovati, D.P. Sellan, C.H. Amon, On the lattice Boltzmann method for phonon transport, J. Comput. Phys. 230 (15) (2011) 5864–5876.
[25] Y. Guo, M. Wang, Lattice Boltzmann modeling of phonon transport, J. Comput. Phys. 315 (2016) 1–15.
[26] Y. Guo, M. Wang, Lattice Boltzmann scheme for hydrodynamic equation of phonon transport, Int. J. Therm. Sci. 171 (2022) 107178.
[27] Z. Guo, K. Xu, Discrete unified gas kinetic scheme for multiscale heat transfer based on the phonon Boltzmann transport equation, Int. J. Heat Mass Transfer 102 (2016) 944–958.
[28] Z. Guo, K. Xu, R. Wang, Discrete unified gas kinetic scheme for all Knudsen number flows: low-speed isothermal case, Phys. Rev. E 88 (3) (2013) 033305.
[29] L. Mieussens, On the asymptotic preserving property of the unified gas kinetic scheme for the diffusion limit of linear kinetic models, J. Comput. Phys. 253 (2013) 138–156.
[30] A. Mittal, S. Mazumder, Hybrid discrete ordinates—spherical harmonics solution to the Boltzmann Transport Equation for phonons for non-equilibrium heat conduction, J. Comput. Phys. 230 (18) (2011) 6977–7001.
[31] Y. Guo, M. Wang, Heat transport in two-dimensional materials by directly solving the phonon Boltzmann equation under Callaway's dual relaxation model, Phys. Rev. B 96 (2017) 134312 -134312.
[32] Y. Guo, M. Wang, Phonon hydrodynamics for nanoscale heat transport at ordinary temperatures, Phys. Rev. B 97 (2018) 035421 -035421.
[33] Y. Huang, M. Wang, Nonnegative magnetoresistance in hydrodynamic regime of electron fluid transport in two-dimensional materials, Phys. Rev. B 104 (15) (2021) 155408.
[34] Y. Hu, Y. Shen, H. Bao, Ultra-efficient and parameter-free computation of submicron thermal transport with phonon Boltzmann transport equation, Fundament. Res. 26 (1) (2022) 1.
[35] Peterson, R., Direct simulation of phonon-mediated heat transfer in a Debye crystal. 1994. 116(4): p. 815-822.
[36] M. Wang, X. Lan, Z. Li, Analyses of gas flows in micro- and nanochannels, Int. J. Heat Mass Transfer 51 (13) (2008) 3630–3641.
[37] M. Wang, Z. Li, Gas mixing in microchannels using the direct simulation Monte Carlo method, Int. J. Heat Mass Transfer 49 (9-10) (2006) 1696–1702.
[38] S. Mazumder, A. Majumdar, Monte Carlo study of phonon transport in solid thin films including dispersion and polarization, J. Heat Transfer 123 (4) (2001) 749–759.
[39] Q. Hao, G. Chen, M.-S. Jeng, Frequency-dependent Monte Carlo simulations of phonon transport in two-dimensional porous silicon with aligned pores, J. Appl. Phys. 106 (11) (2009) 114321.
[40] D.R. Ladiges, J.E. Sader, Frequency-domain Monte Carlo method for linear oscillatory gas flows, J. Comput. Phys. 284 (2015) 351–366.
[41] Y. Wu, M.F. Modest, D.C. Haworth, A high-order photon Monte Carlo method for radiative transfer in direct numerical simulation, J. Comput. Phys. 223 (2) (2007) 898–922.
[42] M.F. Modest, Radiative Heat Transfer, Academic press, Oxford, 2013.
[43] W. Miao, et al., Deviational Monte Carlo scheme for thermal and electrical transport in metal nanostructures, Phys. Rev. B 99 (20) (2019) 205433.
[44] Q. Hao, H. Zhao, Y. Xiao, A hybrid simulation technique for electrothermal studies of two-dimensional GaN-on-SiC high electron mobility transistors, J. Appl. Phys. 121 (20) (2017) 204501.
[45] Q. Hao, et al., Electrothermal studies of GaN-based high electron mobility transistors with improved thermal designs, Int. J. Heat Mass Transfer 116 (2018) 496–506.
[46] Q. Hao, et al., Hybrid electrothermal simulation of a 3-D Fin-Shaped Field-Effect transistor based on GaN nanowires, IEEE Trans. Electron Dev. 65 (3) (2018) 921–927.
[47] X. Ran, Y. Guo, M. Wang, Interfacial phonon transport with frequency-dependent transmissivity by Monte Carlo simulation, Int. J. Heat Mass Transfer 123 (2018) 616–628.
[48] X. Ran, M. Wang, Efficiency improvement of discrete-ordinates method for interfacial phonon transport by Gauss-Legendre integral for frequency domain, J. Comput. Phys. 399 (2019) 108920.
[49] X. Ran, M. Wang, Abnormal thermal boundary resistance of thin films with heat source, Int. J. Heat Mass Transfer 147 (2020) 118941.
[50] J.-P.M. Péraud, N.G. Hadjiconstantinou, Efficient simulation of multidimensional phonon transport using energy-based variance-reduced Monte Carlo formulations, Phys. Rev. B 84 (20) (2011) 205331.
[51] J.-P.M. Péraud, N.G. Hadjiconstantinou, An alternative approach to efficient simulation of micro/nanoscale phonon transport, Appl. Phys. Lett. 101 (15) (2012) 153114.
[52] J. Yu, et al., MFP-based Monte Carlo method for nanostructure phonon transport, ASME 2019 6th International Conference on Micro/Nanoscale Heat and Mass Transfer, American Society of Mechanical Engineers Digital Collection, 2019.
[53] J. Randrianalisoa, D. Baillis, Monte Carlo simulation of steady-state microscale phonon heat transport, J. Heat Transfer 130 (7) (2008) 072404.
[54] S. Cramer, C. Slater, Investigation of radiation effects in Hiroshima and Nagasaki using a general Monte Carlo-discrete ordinates coupling scheme, Nucl. Sci. Eng. 114 (1) (1993) 1–11.
[55] L. Liu, H. Zhang, H. Tan, Monte Carlo discrete curved ray-tracing method for radiative transfer in an absorbing-emitting semitransparent slab with variable spatial refractive index, J. Quant. Spectrosc. Radiat. Transfer 84 (3) (2004) 357–362.
[56] Z. Zheng, et al., Application of a 3D discrete Ordinates-Monte Carlo coupling method to deep-penetration shielding calculation, Nucl. Eng. Des. 326 (2018) 87–96.
[57] G. Chen, Nanoscale Energy Transport and Conversion: A Parallel Treatment of Electrons, Molecules, Phonons, and Photons, Oxford University Press, New York, 2005.
[58] Si. Available from: http://www.ioffe.ru/SVA/NSM/Semicond/Si/mechanic.html.
[59] R. Stedman, G. Nilsson, Dispersion relations for phonons in aluminum at 80 and 300°K, Phys. Rev. 145 (2) (1966) 492–500.
[60] Ge. Available from: http://www.ioffe.ru/SVA/NSM/Semicond/Ge/mechanic.html.
[61] M. Asen-Palmer, et al., Thermal conductivity of germanium crystals with different isotopic compositions, Phys. Rev. B 56 (15) (1997) 9431.
[62] M.G. Holland, Analysis of lattice thermal conductivity, Phys. Rev. 132 (6) (1963) 2461–2471.
[63] N. Mingo, et al., Predicting the thermal conductivity of Si and Ge nanowires, Nano Lett. 3 (12) (2003) 1713–1716.
[64] A.J. Minnich, et al., Quasiballistic heat transfer studied using the frequency-dependent Boltzmann transport equation, Phys. Rev. B 84 (23) (2011) 235207.
[65] A. Majumdar, Microscale heat conduction in lelectnc thin films, J. Heat Transfer 115 (1993) 7–16.
[66] J.-P.M. Péraud, C.D. Landon, N.G. Hadjiconstantinou, Monte Carlo methods for solving the Boltzmann transport equation, Annu. Rev. Heat Transfer 17 (2014) 205–265.
[67] J. Yu, et al., MFP-based Monte Carlo method for nanostructure phonon transport, ASME 2019 6th International Conference on Micro/Nanoscale Heat and Mass Transfer, 2019.
[68] C. Hua, A.J. Minnich, Semi-analytical solution to the frequency-dependent Boltzmann transport equation for cross-plane heat conduction in thin films, J. Appl. Phys. 117 (17) (2015) 175306.